# The inception of star cluster formation revealed by [C ii] emission around an Infrared Dark Cloud

N.B. When citing this work, cite the original published paper.

(article starts on next page)

# The inception of star cluster formation revealed by [C II] emission around an Infrared Dark Cloud

Thomas G. Bisbas,[1,2]★ Jonathan C. Tan,[1,3] Timea Csengeri,[4] Benjamin Wu,[5] Wanggi Lim,[6] Paola Caselli,[2] Rolf Güsten,[4] Oliver Ricken[4] and Denise Riquelme[4]

[1]*Department of Astronomy, University of Virginia, Charlottesville, VA 22904, USA*
[2]*Max-Planck-Institut für Extraterrestrische Physik, Giessenbachstrasse 1, D-85748 Garching, Germany*
[3]*Department of Space, Earth & Environment, Chalmers University of Technology, SE-412 96 Gothenburg, Sweden*
[4]*Max-Planck-Institut für Radioastronomie, auf dem Hügel 69, D-53121 Bonn, Germany*
[5]*National Astronomical Observatory of Japan, Mitaka, Tokyo 181-8588, Japan*
[6]*SOFIA-USRA, NASA Ames Research Center, MS 232-12, Moffett Field, CA 94035, USA*

## ABSTRACT

We present *SOFIA-upGREAT* observations of [C II] emission of Infrared Dark Cloud (IRDC) G035.39-00.33, designed to trace its atomic gas envelope and thus test models of the origins of such clouds. Several velocity components of [C II] emission are detected, tracing structures that are at a wide range of distances in the Galactic plane. We find a main component that is likely associated with the IRDC and its immediate surroundings. This strongest emission component has a velocity similar to that of the $^{13}$CO(2–1) emission of the IRDC, but offset by $\sim 3\,\mathrm{km\,s^{-1}}$ and with a larger velocity width of $\sim 9\,\mathrm{km\,s^{-1}}$. The spatial distribution of the [C II] emission of this component is also offset predominantly to one side of the dense filamentary structure of the IRDC. The C II column density is estimated to be of the order of $\sim 10^{17}$–$10^{18}\,\mathrm{cm^{-2}}$. We compare these results to the [C II] emission from numerical simulations of magnetized, dense gas filaments formed from giant molecular cloud (GMC) collisions, finding similar spatial and kinematic offsets. These observations and modelling of [C II] add further to the evidence that IRDC G035.39-00.33 has been formed by a process of GMC–GMC collision, which may thus be an important mechanism for initiating star cluster formation.

**Key words:** radiative transfer – – ISM: clouds – ISM: kinematics and dynamics .

## 1 INTRODUCTION

Infrared Dark Clouds (IRDCs) are dense parts of molecular clouds, discovered due to their mid-infrared (MIR) absorption of Galactic background light (Pérault et al. 1996; Egan et al. 1998). Their characteristic masses, sizes, and densities indicate that they are likely to be the precursors of star-forming clumps and star clusters (e.g. Tan et al. 2014). Since most stars form in such clusters, the study of IRDCs can thus reveal crucial information on the processes that set global galactic star formation rates. There have been many observational studies of IRDCs (see review by, e.g. Tan et al. 2014). One well-studied sample of IRDCs is that selected by Butler & Tan (2009, 2012), i.e. 10 RDCs (named A–J) for which methods of MIR extinction mapping to measure cloud structure were developed. Kainulainen & Tan (2013) then developed combined near-infrared (NIR) and MIR extinction maps, which more accurately probe the lower column density envelopes of these clouds. Hernandez & Tan

(2015) studied the kinematics and dynamics of these 10 IRDCs and their surrounding giant molecular clouds (GMCs) using $^{13}$CO Galactic Ring Survey (GRS) data (Jackson et al. 2006).

From the above sample of 10 IRDCs, G035.39-00.33 (IRDC H) was mapped in many molecular tracers with the IRAM 30m telescope. This IRDC is a highly filamentary cloud at a near kinematic distance of 2.9 kpc (Simon et al. 2006). These observations detected parsec scale SiO(2–1) emission, which is potentially caused by large-scale shocks due to converging flows and/or a collision of two molecular clouds (Jiménez-Serra et al. 2010; Wu et al. 2015, 2017a, 2017b). These data were also used to discover widespread CO depletion in the dense IRDC filament (Hernandez et al. 2011), as well as constraining filament dynamics (Hernandez et al. 2012), with indications that its inner regions are virialized. Henshaw et al. (2013) found velocity offsets of dense N$_2$H$^+$ emitting gas compared to lower density C$^{18}$O emitting gas. With IRAM PdBI, Henshaw et al. (2014) identified several sub-filaments within IRDC H, analogous to the structures discovered by Hacar et al. (2013) in Taurus. Other studies of this IRDC have included measurement

---

★ E-mail: tbisbas@gmail.com (TGB)

of widespread deuteration (Barnes et al. 2016) and its temperature structure (Sokolov et al. 2017).

To date there have been relatively few previous studies of [C II] from IRDCs. Beuther et al. (2014) studied the carbon cycle (CO, C I, C II) in very localized regions (typically just a few parsecs in size) within several IRDCs using *Herschel-HIFI* for three clouds and *SOFIA-GREAT* for one cloud. [C II] was detected in three regions; the mass of the gas in C II was always higher by a factor of a few than that of C I. Averaging over these regions, the [C II] lines were observed to be relatively broad ($\gtrsim 10\,\mathrm{km\,s^{-1}}$) and with integrated intensities of several K km s$^{-1}$. While the [C II] emission depends on the strength of the radiation field, they also found additional signatures of multiple velocity components and strong velocity gradients that indicate that other processes, e.g. energetic gas flows, may also be contributing to the [C II] excitation and perhaps be involved in the formation of IRDCs.

In this Letter, we present pilot [C II] *SOFIA-upGREAT* observations of IRDC H, with the primary goal of understanding the lower density atomic layers around the dense gas structure to constrain models of the formation conditions of such clouds and thus the initiation of star cluster formation.

## 2 OBSERVATIONS

We obtained a fully sampled map of the 158 μm atomic fine structure line of [C II] with the upGREAT receiver (Risacher et al. 2016) on-board *SOFIA* on 2016 May 18 as part of the program 04_0169 (PI: Tan). The upGREAT array was tuned to the [C II] line at 1900.537 GHz in the lower sideband using both the H and V polarizations and the OTF mode. The low-frequency channel was tuned to the $^{12}$CO(11–10) line at 1267.0 GHz in the lower sideband of the receiver. The observations were carried out at an altitude of 43 kft for a total on-source integration time of ∼33 min and with an atmospheric water vapour content below 10 μm, resulting in an atmospheric opacity of 0.18–0.22 at the frequency of the [C II] line. An OFF position of $l = 35.6987°$, $b = -0.6019°$ was used. The data were calibrated with the KOSMA/GREAT calibrator (Guan et al. 2012), and further processed with the CLASS software. The overall absolute flux calibration is expected to be within the nominal 10 per cent uncertainty.

The spectra were converted to the $T_{\mathrm{mb}}$ temperature scale with a main beam efficiency determined for each pixel based on observations of Jupiter. The average efficiency is $\langle\eta_{\mathrm{mb}}^{\mathrm{LFA}}\rangle = 0.65$ for the upGREAT array, and $\langle\eta_{\mathrm{mb}}^{\mathrm{L1}}\rangle = 0.66$ for the L1 channel. We then processed the $^{12}$CO(11–10) and the [C II] data in the same way. A third-order baseline was subtracted from each spectrum, excluding the velocity range of the [C II] emission averaged over the map. The beam is 17.3 arcsec for the $^{12}$CO(11–10), and 14.8 arcsec for the [C II] observations, respectively, and the spectra were gridded using a sampling of 1/3 of the beam for both lines. The maps extend over an area of 360 arcsec × 520 arcsec, covering the main part of the IRDC filament as well as its immediate surroundings. We measure a noise level of 0.5 K in a single beam for the [C II] line in 0.3 km s$^{-1}$ velocity bins, and 1.04 K for the $^{12}$CO(11–10) line in the lowest noise part of the spectrum. The $^{12}$CO(11–10) line is not detected, therefore in the following we focus on the [C II] data.

## 3 RESULTS

In Fig. 1 we show the [C II] spectrum averaged over the observed region. Several emission peaks are seen. The strongest has a $v_{\mathrm{lsr}}$ of about 48 km s$^{-1}$. Other emission is seen over a broad velocity range,
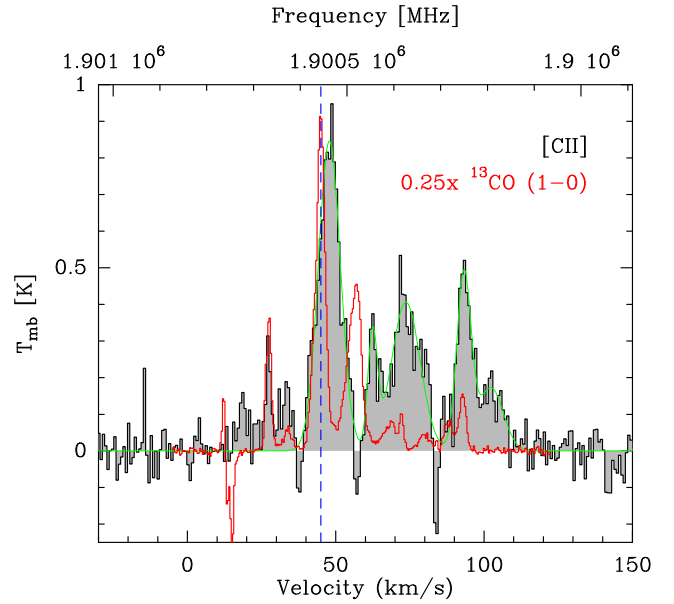


**Figure 1.** Grey filled histogram shows the [C II] spectrum averaged over the entire mapped region of IRDC H. The GRS $^{13}$CO(1–0) spectrum averaged over the same region is shown in red. The upper *x*-axis shows the signal band frequency scale for the [C II] data. For better visibility, the $^{13}$CO spectrum is scaled by a factor of 0.25. The blue dashed line shows $v_{\mathrm{lsr}}$ of the IRDC.

including weak features at ∼30 km s$^{-1}$ and relatively strong features up to ∼110 km s$^{-1}$. We note that the observed negative features, e.g. near 70 km s$^{-1}$ and possibly near 38 and 57 km s$^{-1}$, are likely from contamination of [C II] emission in the OFF position. We fit five Gaussian components to the spectrum and list the results in Table 1. Fig. 1 also shows the $^{13}$CO(1–0) spectrum obtained by the GRS (Jackson et al. 2006) over the same region. The $v_{\mathrm{lsr}}$ of the IRDC is at ∼45 km s$^{-1}$ as determined from this $^{13}$CO(1–0) emission (e.g. Hernandez & Tan 2015), and this is within about 3 km s$^{-1}$ of the brightest [C II] emission feature. In the velocity range $v_{\mathrm{lsr}}$ ∼ 39.7– 49.9 km s$^{-1}$, Hernandez & Tan (2015) find that the highest peaks of brightness temperature of $^{13}$CO(1-0) are associated with IRDC H, however there is also significant contribution from the surrounding GMC. For the velocity range 49.9–62.6 km s$^{-1}$, which corresponds to the second highest peak in $^{13}$CO emission in Fig. 1, they find an extended GMC-scale component that is connected in position– velocity space to the 45 km s$^{-1}$ feature, of which a significant part overlaps on the same line of sight as IRDC H. This indicates that this filamentary IRDC may have been formed as a result of an ongoing cloud–cloud collision.

Fig. 2 shows the integrated emission of [C II] (in the 40–55 km s$^{-1}$ velocity range) and 8 μm emission map of that area. IRDC H is seen as a dark filamentary structure, indicating high extinction and therefore high column densities with respect to the surrounding medium. These maps reveal a spatial offset between the [C II] emitting gas and the highest column density regions of the IRDC. The other components of the spectra are not well detected in the individual beams, suggesting that they originate from a more diffuse Galactic foreground or background.

We calculate the column density of C II in the optically thin limit for the component associated with the IRDC. Following Goldsmith et al. (2012) (see also Beuther et al. 2014), the column density,

**Table 1.** Parameters for fitted Gaussian components to the [C II] spectrum shown in Fig. 1. Columns from left to right: velocity along the line of sight ($v_{lsr}$), velocity width ($\Delta v$), peak brightness temperature ($T_{mb}$), and velocity integrated $T_{mb}$ ($\int T_{mb}\, dv$).

| $v_{lsr}$ (km s$^{-1}$) | $\Delta v$ (km s$^{-1}$) | $T_{mb}$ (K) | $\int T_{mb}\, dv$ (K km s$^{-1}$) |
|---|---|---|---|
| $47.87 \pm 0.16$ | $8.76 \pm 0.36$ | $0.85 \pm 0.05$ | $7.89 \pm 0.28$ |
| $62.44 \pm 0.32$ | $3.82 \pm 0.82$ | $0.31 \pm 0.09$ | $1.26 \pm 0.25$ |
| $73.65 \pm 0.41$ | $11.39 \pm 0.97$ | $0.41 \pm 0.05$ | $4.92 \pm 0.36$ |
| $93.22 \pm 0.34$ | $5.67 \pm 0.82$ | $0.48 \pm 0.10$ | $2.89 \pm 0.47$ |
| $102.31 \pm 1.26$ | $9.84 \pm 3.23$ | $0.17 \pm 0.08$ | $1.81 \pm 0.52$ |
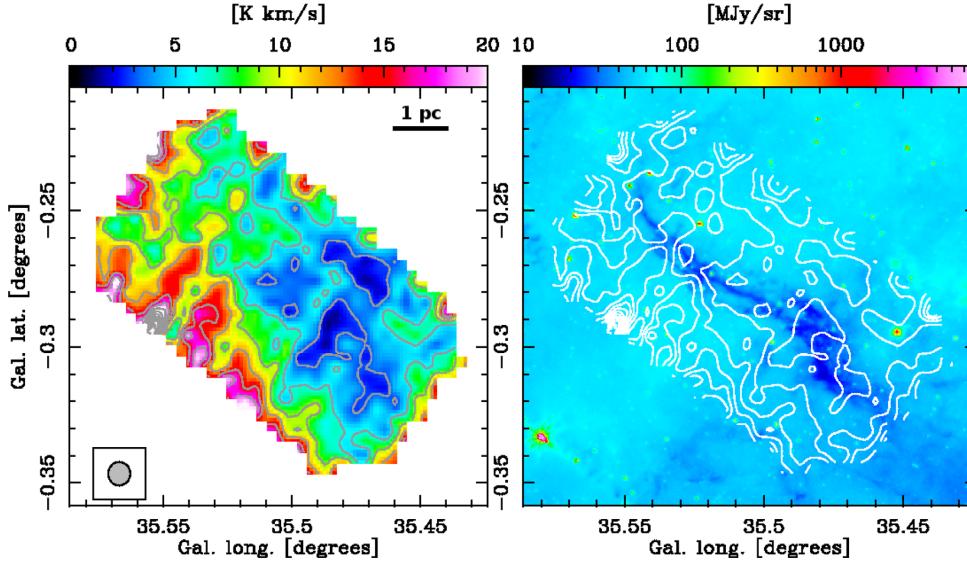


**Figure 2.** *Left:* Integrated emission of [C II] between 40 and 55 km s$^{-1}$ corresponding to the brightest velocity component close to the $v_{lsr}$ of IRDC H. To achieve a better signal-to-noise, we smoothed the map to 31 arcsec. The beam is shown in the lower left panel. A linear scale of 1 pc for an adopted distance of 2.9 kpc is shown. *Right: Spitzer* 8 μm map of the region. IRDC H is seen in absorption against the Galactic background. White contours show the velocity integrated [C II] emission and are the same as in the left-hand panel.

$N$(C II), is given by the expression

$$N(\text{C\,II}) = \frac{10^{16}}{3.43}\left[1 + 0.5e^{91.25/T_{kin}}\left(1 + \frac{2.4\times10^{-6}}{C_{ul}}\right)\right]$$
$$\times \int T_{mb}\, dv, \tag{1}$$

where $T_{kin}$ is the gas temperature and $C_{ul}$ is the collision rate. The integrated emission of the spectrum of the main component is $\int T_{mb}\, dv \sim 7.89$ K km s$^{-1}$ (see Table 1). $C_{ul}$ depends primarily on the collisions with H and H$_2$. For an average gas temperature of $T_{kin} \sim 160$ K [a reasonable value for photodissociation region (PDR) models, and being close to the average value we derive in our theoretical modelling below], and an H-nucleus number density in the range of $10^2$–$10^3$ cm$^{-3}$, we obtain a column density in the order of $N(\text{CII}) \sim 10^{17}$–$10^{18}$ cm$^{-2}$.

PDR modelling shows that [C II] is primarily emitted from lower density regions when they interact with far-ultraviolet (FUV) radiation from nearby stars (e.g. Röllig et al. 2007). In regions of higher extinction, such as the densest part in the right-hand panel of Fig. 2, the FUV radiation is severely extinguished and thus [C II] diminishes, unless very strong shocks or very high cosmic ray ionization rates are present, (e.g. Meijerink et al. 2011; Bisbas, Papadopoulos & Viti 2015; Bisbas et al. 2017a). However, these are not expected in the case of IRDC H, given its location in the Galaxy.

We compare our IRDC H data with GOT C+ data from the *Herschel* archive (Pineda et al. 2013; Langer et al. 2014) of nine surrounding regions (see Fig. 3). Assuming a ~2.9 kpc distance, i.e. the near kinematic implied by the velocity of IRDC H, we find that the closest *Herschel* observation is located ~22 pc away (G035.1+0.0). Interestingly, $T_{mb}$ peaks at ~45 km s$^{-1}$. This indicates a possible larger scale connection, meaning that the GMC atomic envelope extends in that direction, which is in agreement with the $^{13}$CO(1–0) data analysed by Hernandez & Tan (2015) for that wider region. This $T_{mb}$ peak is also seen at the G035.1+0.5 *Herschel* observation, however it is not possible to unambiguously demonstrate a connection of IRDC H to that location. The velocity peak at $v_{lsr} \sim 90$ km s$^{-1}$ that we obtain from our data is possibly connected with the kinematics of the spiral structure of our Galaxy. This is supported from similar high velocities that are seen in GOT C+ data and in particular in the objects with Galactic latitude of $-0.5 \lesssim b \lesssim 0.5$, contrary to those in higher latitude (see the lower panels of Fig. 3).

## 4  THEORETICAL MODELLING

We perform a 3D-PDR (Bisbas et al. 2012) modelling of subregions extracted from magnetohydrodynamic (MHD) simulations of GMCs (Wu et al. 2017a). We note that we are not attempting to model the specific structure of IRDC H, but to understand the nature of [C II] emission from similar dense structures that form via cloud collisions or decay of turbulence in self-gravitating clouds. We consider two cases: (i) a GMC–GMC collision at a relative speed of 10 km s$^{-1}$ (Model 1 of Wu et al. at $t = 4$ Myr); (ii) two overlapping but non-colliding GMCs along the line of sight. The
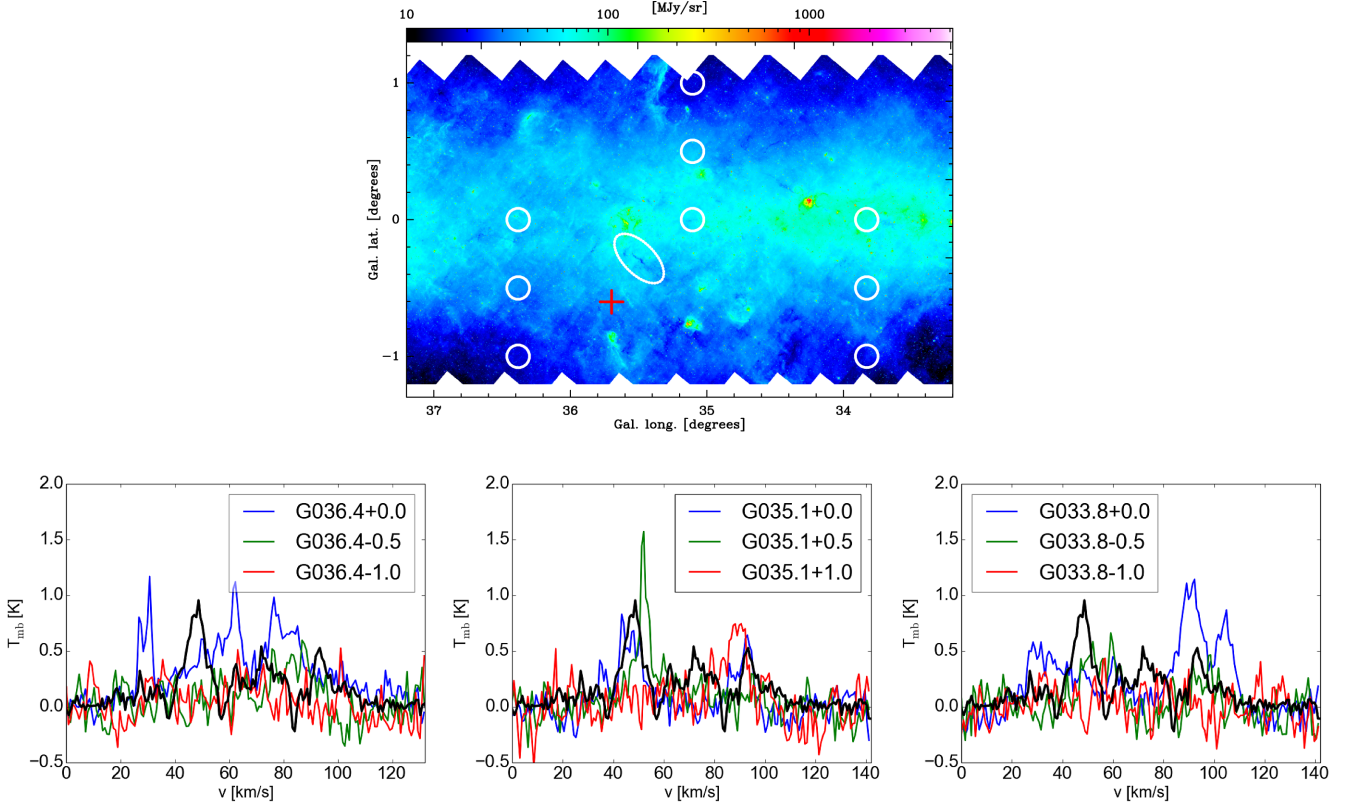
**Figure 3.** *Top panel:* An extended map at 8 μm showing the area surrounding IRDC H in the Galactic plane. The centre of each white circle is *Herschel's* [C II] observations (GOT C+ Pineda et al. 2013; Langer et al. 2014). The white ellipse indicates the position of IRDC H, which is close to the G035+0.0 GOT C+ observation. The red cross shows the OFF position of our observations. *Bottom row:* Blue, green, and red solid lines correspond to the GOT C+ observations of [C II] 158 μm for the nine nearby regions to IRDC H. The solid black line in each panel shows the *SOFIA* [C II] data towards IRDC H.

selected subregions from the MHD simulations have volumes of $12^3$ pc$^3$ and, for the case of the colliding GMCs, it contains the highest density part of the cloud, i.e. formed as a direct result of the collision. In this first case, the high-density structure has a linear size of $\lesssim 7$ pc, comparable to the size of IRDC H ($\sim$5 pc). We orient it so that the direction of collision is along the line of sight, which maximizes $v_{lsr}$ offsets that result from the collision (Bisbas et al. 2017b). After some experimentation involving comparing total integrated intensities of [C II] emission with the observed region, for both the simulations shown we used an isotropic FUV radiation field of $\chi/\chi_0 = 10$ (normalized relative to Draine 1978) and a cosmic ray ionization rate of $\zeta_{CR} = 10^{-16}$ s$^{-1}$. This few-times-enhanced FUV intensity (Wolfire et al. 2003) may indicate possible nearby star formation activity, which is also consistent with relatively bright 8 μm emission in the surroundings (Fig. 3).

The left column of Fig. 4 shows the integrated intensity map of [C II] for the colliding scenario (top panel), and the non-colliding scenario (bottom panel), without considering any observational or instrumental effects. Contours show the highest peaks of total H-nucleus column density, $N_H$. We find that these are offset when compared to the peaks of [C II] emission only in the GMC–GMC collision simulation. This is in qualitative agreement with our observations, indicating that the observed [C II] originates from the surrounding medium and not from the dense filament itself.

The right column of Fig. 4 shows the average velocity spectrum of the entire analysed region of the clouds (top panel: colliding scenario; bottom panel: non-colliding scenario). The red line corresponds to the [C II] emission and the green line to the $^{12}$CO $J = 1$–0

emission (we note that $^{13}$CO is not yet treated in the 3D-PDR code, so we use $^{12}$CO as its proxy). In the first case, we find a velocity offset of 2.7 km s$^{-1}$ between the average ($T_{mb}$-weighted) velocities of [C II] and $^{12}$CO and about a 1.1 km s$^{-1}$ offset between the peaks of these spectra. These offsets are similar to those observed between [C II] and $^{13}$CO towards IRDC H. The range of the [C II] velocity distribution is about 10 km s$^{-1}$ with a dispersion of 4.1 km s$^{-1}$. The $^{12}$CO emission is distributed over a similar range of velocities. Note that $^{13}$CO is expected to be more localized in velocity space, given that it traces denser conditions. The velocity offset and dispersion of the [C II] and $^{13}$CO in this theoretical model are broadly consistent with those seen in IRDC H. On the other hand, the non-colliding case has a much smaller velocity offset, i.e. the $T_{mb}$-weighted average velocities of [C II] and $^{12}$CO are both $\lesssim 0.4$ km s$^{-1}$ and the offset between the peaks of these spectra is $\sim$0.5 km s$^{-1}$. These results thus support the scenario that IRDC H is a result of the collision between GMCs.

## 5 DISCUSSION AND CONCLUSIONS

We have presented *SOFIA-upGREAT* observations of [C II] 158 μm emission of a well-studied filamentary IRDC. We find that the integrated emission of [C II] is spatially offset compared to the dense structure of the IRDC, as seen in absorption at 8 μm against the Galactic background. An offset in velocity of about 3 km s$^{-1}$ is also seen when comparing [C II] with $^{13}$CO(1–0) emission. The velocity dispersion of the [C II] component is about 9 km s$^{-1}$, a few times broader than that of the $^{13}$CO(2–1) emission from the IRDC.
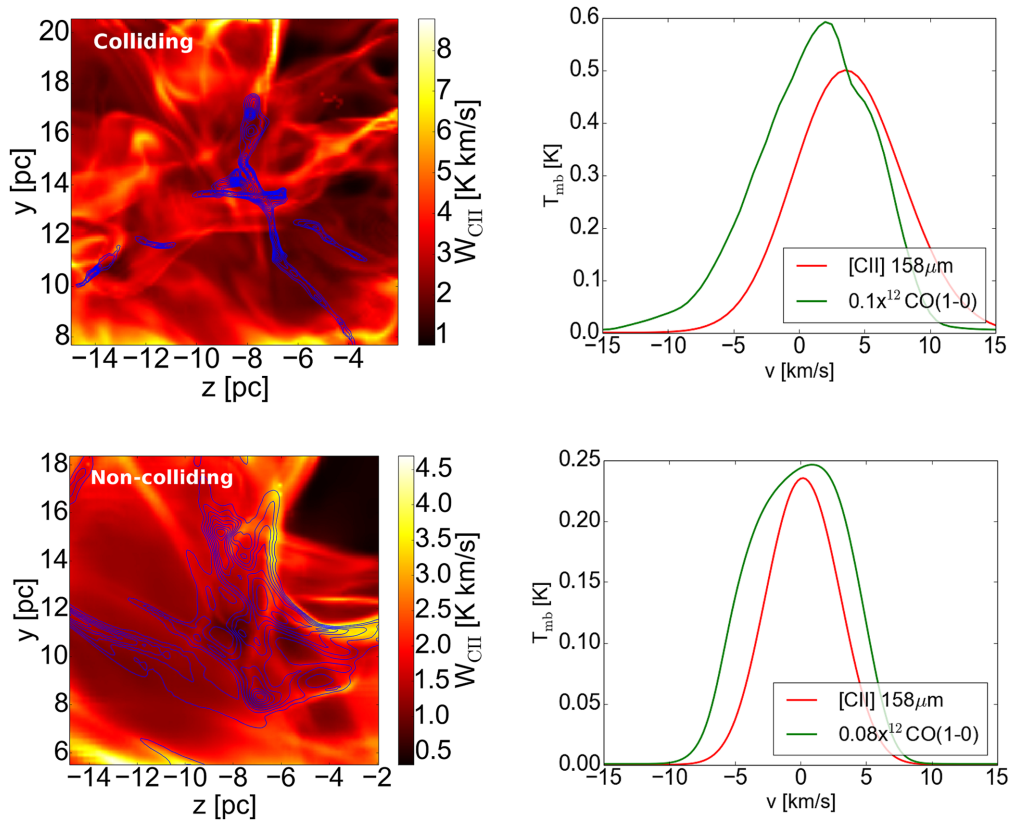
**Figure 4.** Synthetic observations of a subregion from the MHD simulation by Wu et al. (2017a) of two colliding (top row) and non-colliding (bottom row) GMCs that are along the line of sight of the observer. The left column shows the [C II] emission whereas the blue contours indicate the highest peaks of the total H-nucleus column density. In the colliding case, there is an offset of a few pc between [C II] emission and the column density peaks, in qualitative agreement with our observations of IRDC H. In the non-colliding case, we do not find such an offset. The right column shows the average velocity spectrum of [C II] and $^{12}$CO J = 1–0 lines. In the colliding case, we find an offset in the $T_{mb}$-weighted average velocities of these two lines of about 2.7 km s$^{-1}$. In the non-colliding case, this offset is $\lesssim 0.4$ km s$^{-1}$.

The column density of C II of the main component in the optically thin limit is found to be in the order of $N_{C\,II} \sim 10^{17}$–$10^{18}$ cm$^{-2}$, assuming an average gas kinetic temperature of $\sim$160 K, derived from our theoretical modelling. A similar component of [C II] emission is seen in a nearby region, 22 pc away to the north-west, from *Herschel*-GOTC+ data, but not in the opposite direction. However, in the local map obtained by *SOFIA*, the [C II] emission is stronger in a direction to the east.

A primary $T_{mb}$ peak in $^{13}$CO(1–0) is observed at $v_{lsr} \sim 45$ km s$^{-1}$, while a secondary one is observed at $v_{lsr} \sim 55$ km s$^{-1}$. Such a difference of $\sim$10 km s$^{-1}$, together with their known connection in position–velocity space (Hernandez & Tan 2015) and the observed widespread SiO(2–1) emission (Jiménez-Serra et al. 2010), strengthens the GMC–GMC collision scenario as the most probable formation mechanism of IRDC H. This is the first such example of a GMC collision producing dense gas that likely leads to star cluster formation.

Using 3D-PDR, we post-processed sub-regions of MHD simulations of two colliding and non-colliding GMCs, presented in Wu et al. (2017a). The simulated [CII] velocity integrated emission maps of the colliding scenario show a spatial offset when compared to the total H-nucleus column density and are thus in qualitative agreement with the *SOFIA* observations of the IRDC. Here, a velocity offset is present in the simulated spectra, similar to the one observed in the IRDC. In the context of a GMC–GMC collision scenario for the formation of IRDC H, this demonstrates consistency with the adopted parameters of a 10 km s$^{-1}$ collision speed, which is also supported by the observed $^{13}$CO(1–0) components. These features are either minimized or not observed in the non-colliding GMCs simulation, supporting the fact that the IRDC H may have formed as a result of a cloud–cloud collision.

There are still alternative possibilities to the above. For example, the [C II] emission may simply trace the turbulent boundary region of a massive GMC or GMC complex, of which IRDC H only represents one small part, however mapping of a larger region around the IRDC is needed. Higher sensitivities are also needed to enable higher resolution spatial mapping of the [C II] emission. Such observations can help improve our understanding of IRDC formation and thus the processes that initiate star cluster formation and control the star formation rates of galaxies.

# REFERENCES

Barnes A. T., Kong S., Tan J. C., Henshaw J. D., Caselli P., Jimnez-Serra I., Fontani F., 2016, MNRAS, 458, 1990

Beuther H. et al., 2014, A&A, 571, A53

Bisbas T. G., Bell T. A., Yates J., Barlow M. J., 2012, MNRAS, 427, 2100

Bisbas T. G. , Papadopoulos P. P., Viti S., 2015, ApJ, 803, 37

Bisbas T. G., van Dishoeck E. F., Papadopoulos P. P., Szűcs L., Bialy S., Zhang Z.-Y., 2017a, ApJ, 839, 90

Bisbas T. G., Tanaka K. E. I., Tan J. C., Wu B., Nakamura F., 2017b, ApJ, 850, 23

Butler M. J., Tan J. C., 2009, ApJ, 696, 484

Butler M. J., Tan J. C., 2012, ApJ, 754, 5

Draine B. T., 1978, ApJS, 36, 595

Egan M. P., Shipman R. F., Price S. D., Carey S. J., Clark F. O., Cohen M., 1998, ApJ, 494, L199

Goldsmith P. F., Langer W. D., Pineda J. L., Velusamy T., 2012, ApJS, 203, 13

Guan X., Stutzki J., Graf U. U., Gäusten R., Okada Y., Requena-Torres M. A., Simon R., Wiesemeyer H., 2012, A&A, 542, L4

Hacar A., Tafalla M., Kauffmann J., Kovács A., 2013, A&A, 554, A55

Henshaw J. D., Caselli P., Fontani F., Jim´enez-Serra I., Tan J. C., Hernandez A. K., 2013, MNRAS, 428, 3425

Henshaw J. D., Caselli P., Fontani F., Jim´enez-Serra I., Tan J. C., 2014, MNRAS, 440, 2860

Hernandez A. K., Tan J. C., 2015, ApJ, 809, 154

Hernandez A. K., Tan J. C., Caselli P., Butler M. J., Jim´enez-Serra I., Fontani F., Barnes P., 2011, ApJ, 738, 11

Hernandez A. K., Tan J. C., Kainulainen J., Caselli P., Butler M. J., Jim´enez-Serra I., Fontani F., 2012, ApJ, 756, L13

Jackson J. M. et al., 2006, ApJS, 163, 145

Jiménez-Serra I., Caselli P., Tan J. C., Hernandez A. K., Fontani F., Butler M. J., van Loo S., 2010, MNRAS, 406, 187

Kainulainen J., Tan J. C., 2013, A&A, 549, A53

Langer W. D., Velusamy T., Pineda J. L., Willacy K., Goldsmith P. F., 2014, A&A, 561, A122

Meijerink R., Spaans M., Loenen A. F., van der Werf P. P., 2011, A&A, 525, A119

Pérault M. et al., 1996, A&A, 315, L165

Pineda J. L., Langer W. D., Velusamy T., Goldsmith P. F., 2013, A&A, 554, A103

Risacher C. et al., 2016, A&A, 595, A34

Röllig M. et al., 2007, A&A, 467, 187

Simon R., Jackson J. M., Rathborne J. M., Chambers E. T., 2006, ApJ, 639, 227

Sokolov V. et al., 2017, A&A, 606, A133

Tan J. C., Beltrán M. T., Caselli P., Fontani F., Fuente A., Krumholz M. R., McKee C. F., Stolte A., 2014 in Beuther H., Klessen R. S., Dullemond C. P., Henning T., eds, Protostars and Planets VI. Univ. Arizona Press, Tucson, AZ,p. 149

Wolfire M. G., McKee C. F., Hollenbach D., Tielens A. G. G. M., 2003, ApJ, 587, 278

Wu B., Van Loo S., Tan J. C., Bruderer S., 2015, ApJ, 811, 56

Wu B., Tan J. C., Nakamura F., Van Loo S., Christie D., Collins D., 2017a, ApJ, 835, 137

Wu B., Tan J. C., Christie D., , Nakamura F., Van Loo S., Collins D., 2017b, ApJ, 841, 88

This paper has been typeset from a TEX/LATEX file prepared by the author.